

THE REST-FRAME OPTICAL MORPHOLOGY OF EMISSION LINE GALAXIES AT $2 \lesssim z \lesssim 3$:
EVIDENCE FOR INSIDE-OUT GALAXY FORMATION IN LOW-MASS GALAXIESALEX HAGEN^{1, 2}, NICHOLAS A. BOND³, ROBIN CIARDULLO^{1, 2}, CARYL GRONWALL^{1, 2}, ERIC GAWISER⁴, WILLIAM BOWMAN^{1, 2},
JOANNA S. BRIDGE^{1, 2}, HENRY S. GRASSHORN GEBHARDT^{1, 2}, AND DONALD P. SCHNEIDER^{1, 2}*ApJ, Submitted*

ABSTRACT

We compare the rest-frame ultraviolet and rest-frame optical morphologies of $2 \lesssim z \lesssim 3$ star-forming galaxies in the GOODS-S field using *Hubble Space Telescope* WFC3 and ACS images from the CANDELS, GOODS, and ERS programs. We show that the distribution of sizes and concentrations for $1.90 < z < 2.35$ galaxies selected via their rest-frame optical emission-lines are statistically indistinguishable from those of Ly α emitting systems found at $z \sim 2.1$ and $z \sim 3.1$. We also show that the $z \gtrsim 2$ star-forming systems of all sizes and masses become smaller and more compact as one shifts the observing window from the UV to the optical. We argue that this offset is due to inside-out galaxy formation over the first ~ 2 Gyr of cosmic time.

Subject headings: cosmology: observations — galaxies: formation — galaxies: high-redshift — galaxies: structure

1. INTRODUCTION

The majority of galaxies in the local universe lie on the Hubble sequence (Hubble 1936), a continuum that runs from red, passively-evolving compact ellipticals to gas-rich, star-forming disks with exponential surface brightness profiles. This morphological sequence is clearly visible out to intermediate redshifts (e.g., Glazebrook et al. 1995; van den Bergh et al. 1996; Griffiths et al. 1996; Brinchmann et al. 1998; Lilly et al. 1998; Simard et al. 1999; van Dokkum et al. 2000; Stanford et al. 2004; Ravindranath et al. 2004), but by $z \sim 2$ the relationship breaks down (e.g., Giavalisco et al. 1996; Lowenthal et al. 1997; Dickinson 2000; van den Bergh 2001; Papovich et al. 2005; Conselice et al. 2005; Pirzkal et al. 2007). In fact, a number of surveys have demonstrated that most star-forming galaxies between $2 \lesssim z \lesssim 3$ are clumpy, disturbed, or disk-like, and only $\sim 30\%$ have surface brightness profiles consistent with galactic spheroids (e.g., Ferguson et al. 2004; Elmegreen & Elmegreen 2005; Lotz et al. 2006; Ravindranath et al. 2006; Petty et al. 2009; Tacchella et al. 2015). These studies also show that the typical half-light radii of star-forming galaxies at $z \gtrsim 2$ is ~ 2 kpc, and that their sizes evolve approximately as $H^{-1}(z)$.

There are two limitations to the analyses cited above. The first is associated with the wavelength of observation. To date, most morphological surveys of $z \gtrsim 2$ galaxies have been conducted in the rest-frame ultraviolet, where light from newly-born stars dominates. This limitation can have a profound effect on the results, as in the nearby universe, galaxies become less concentrated, more clumpy, and more asymmetric as one shifts the observing window from the red and infrared to the ultra-

violet (e.g., Taylor-Mager et al. 2007). Consequently, to properly compare the morphology of $z \gtrsim 2$ galaxies to systems in the local universe, one must move from the rest-frame UV to (at least) the rest-frame optical. Only recently have there been investigations of this type (e.g., Bond et al. 2011; Patel et al. 2013; Lang et al. 2014; van der Wel et al. 2014).

A second limitation of most morphological analyses arises from the galaxy sample selection. Most studies of $z \gtrsim 2$ systems have focused on objects that were identified, at least in part, on the basis of their continuum brightness. This criterion creates a bias in favor of high stellar-mass objects located on the bright end of galaxy luminosity function. Lower-mass objects, which represent the bulk of the epoch's galaxies, have not been well-represented.

In this investigation, we address these two problems using images from the *Hubble Space Telescope's* (HST) Wide Field Camera 3 (WFC3) and the Advanced Camera for Surveys (ACS) that were taken as part of the Cosmic Assembly Near-IR Deep Extragalactic Legacy Survey (CANDELS), the Great Observatories Origin Deep Survey (GOODS), and the WFC3 Early Release Science (ERS) Program (Giavalisco et al. 2004; Windhorst et al. 2011; Grogin et al. 2011; Koekemoer et al. 2011). Our targets for study are $2 \lesssim z \lesssim 3$ star-forming galaxies in the GOODS-S Field, which have been identified via their emission lines, either in the rest-frame optical (oELGs) or through Ly α (LAEs). Because the multi-wavelength HST surveys of this region extend from the UV through the near-IR and reach as deep as $m_{AB} \sim 26.4$ in the F160W (*H*) band, we can probe the morphology of $z \gtrsim 2$ systems in the rest-frame optical, and compare their structure to that measured in the rest-frame UV. Moreover, by analyzing sets of emission-line galaxies drawn from the entire range of stellar masses, we can examine how the systematics of morphology depend on mass.

In §2 we begin by describing the galaxy samples used in this study. In §3 and 4, we summarize the properties of the images and describe the analysis techniques used in our comparative study. In §5, we present the rest-frame

¹ Department of Astronomy and Astrophysics, Pennsylvania State University, University Park, PA 16802, USA

² Institute for Gravitation and the Cosmos, Pennsylvania State University, University Park, PA 16802, USA

³ Cosmology Laboratory (Code 665), NASA Goddard Space Flight Center, Greenbelt, MD 20771, USA

⁴ Physics and Astronomy Department, Rutgers University, Piscataway, NJ 08854, U.S.A.

optical sizes and concentration indices of our galaxies, and compare these data to similar measurements made at shorter wavelengths. In §6, we discuss the implications of our findings.

Throughout this paper, we assume a concordance cosmology with $H_0 = 70 \text{ km s}^{-1} \text{ Mpc}^{-1}$, $\Omega_M = 0.3$, and $\Omega_\Lambda = 0.7$ (Bennett et al. 2013). With these values, $1'' = 8.320 \text{ kpc}$ at $z = 2.1$ and 7.625 kpc at $z = 3.1$.

2. THE GALAXY SAMPLES

The first step towards understanding the morphological systematics of $z \gtrsim 2$ star-forming galaxies is to select a sample of objects representative of the epoch. This process is not straightforward. High-redshift galaxies identified on the basis of their rest-frame UV or optical continuum brightness (i.e., Lyman-break and BzK galaxies; Giavalisco 2002; Daddi et al. 2004) or thermal dust properties (*Herschel* PACS objects, e.g., Rodighiero et al. 2011) are generally high-mass systems destined to become today's giant ellipticals (e.g., Adelberger et al. 2005; Quadri et al. 2007). The best way to reach galaxies further down the mass function is to identify systems from their emission lines, which are excited either by recombination or collisions. In particular, studies of $z \gtrsim 2$ star-forming galaxies have demonstrated that objects selected on the basis of their Ly α or [O III] $\lambda 5007$ line-strength can span an extremely wide range of stellar mass, from $7.5 \lesssim \log M/M_\odot \lesssim 10.5$ (Hagen et al. 2014, 2016).

For our examination of rest-frame optical morphologies, we therefore used three samples of $z \gtrsim 2$ emission-line galaxies in the GOODS-S field. The first set of objects consists of star-forming galaxies identified via their rest-frame optical emission lines, which we call oELGs. Data from the WFC3 G141 grism are ideal for this purpose, and are available in GOODS-S as a consequence of the 3D-HST survey (Brammer et al. 2012). By visually examining these frames, Zeimann et al. (2014) identified a sample of 64 objects in GOODS-S with multiple emission lines, unambiguous redshifts between $1.90 < z < 2.35$, and F125W + F160W continuum magnitudes brighter than $m_{AB} = 26$. An analysis of the galaxies' spectral energy distributions (SEDs) demonstrates that these objects have a very wide range of stellar masses ($7.5 \lesssim \log M/M_\odot \lesssim 10.5$), star formation rates ($1 \lesssim M_\odot \text{ yr}^{-1} \lesssim 500$) and stellar reddening ($0 \lesssim E(B - V) \lesssim 0.4$) (Hagen et al. 2016; Grasshorn Gebhardt et al. 2016).

Our second sample is chosen from the set of $z \sim 2.1$ Ly α emitters identified by Guaita et al. (2010) via deep, narrow-band [O II] $\lambda 3727$ images taken with the Mosaic CCD camera on the Blanco 4-m telescope. These data, which are part of the Multiwavelength Survey by Yale-Chile (MUSYC; Gawiser et al. 2006), are defined to have Ly α rest-frame equivalent widths $\text{EW}_0 > 20 \text{ \AA}$ and Ly α line fluxes greater than $F_{\text{Ly}\alpha} > 2 \times 10^{-17} \text{ ergs cm}^{-2} \text{ s}^{-1}$, or, equivalently, Ly α emission line-luminosities greater than $\log L(\text{Ly}\alpha) > 41.8 \text{ ergs s}^{-1}$ (Ciardullo et al. 2012). Originally, Guaita et al. (2010) discovered 250 LAE candidates over a $\sim 0.3 \text{ deg}^2$ region of the Extended Chandra Deep Field South (ECDF-S; Giacconi et al. 2001); however, after excluding those objects located outside the range of deep *HST* imaging, positioned within 40 pixels

of the edge of a CANDELS image, superposed within $2''$ of a cataloged X-ray source (Lehmer et al. 2005; Virani et al. 2006; Luo et al. 2008), or projected onto a region with an obvious image defect, this $z \sim 2.1$ sample reduces to a set of 24 objects. Like the oELGs described above, this set of LAEs span a very wide range of stellar mass, from $\log M/M_\odot \sim 7.3$ to $\log M/M_\odot \sim 9.5$ (Vargas et al. 2014).

Finally, to supplement the $z \sim 2$ LAEs, we included two sets of $z \sim 3$ Ly α emitters identified via narrow-band [O III] $\lambda 5007$ imaging with the Mosaic camera of the Blanco telescope (Gronwall et al. 2007; Ciardullo et al. 2012). These galaxies, which were also selected to have rest-frame Ly α equivalent widths greater than 20 \AA , have slightly larger Ly α line luminosities than the $z \sim 2.1$ LAEs ($L(\text{Ly}\alpha) > 42.1$ and 42.3 ergs s^{-1} for the Gronwall et al. (2007) and Ciardullo et al. (2012) samples, respectively), but roughly the same median stellar mass (Gawiser et al. 2007; Acquaviva et al. 2011). A total of 20 of these $z \sim 3.1$ galaxies have deep *HST* imaging.

Before analyzing these samples, one additional criterion must be satisfied. Bond et al. (2009) has shown that morphological analyses of high-redshift galaxies cannot be performed at the image sensitivity limit. While Bond et al. (2009) used a signal-to-noise ratio of 30 in their analyses, we adopt a minimum signal-to-noise ratio of 10, while keeping track of the increased uncertainties associated with these lower signal-to-noise measurements. With this restriction, our samples reduce to 23 LAEs at $z \sim 2.1$, 12 LAEs at $z \sim 3.1$, and 61 oELGs with $1.90 < z < 2.35$.

3. THE IMAGES

The source material for our study are the optical through near-IR images taken as part of the CANDELS (Grogin et al. 2011; Koekemoer et al. 2011), GOODS (Giavalisco et al. 2004), and WFC3 ERS programs (Windhorst et al. 2011). Of primary use are the F160W frames from the IR arm of WFC3. These *H*-band data, which have a (drizzled) image scale of $0''.06$ per pixel and a limiting magnitude of $m_{AB} \sim 27.2$, sample the rest-frame optical of our $z \gtrsim 2$ emission-line galaxies extremely well. For $1.90 < z < 2.35$ oELGs, the rest-frame wavelengths covered by the filter go from roughly 4800 \AA to 5800 \AA for galaxies at the blue end of the redshift window, and from $\sim 4200 \text{ \AA}$ to $\sim 5000 \text{ \AA}$ for our highest-redshift objects. For the $z \sim 2.1$ LAEs, the bandpass of the filter extends from 4500 \AA to 5500 \AA , while for the $z \sim 3.1$ LAEs, the range is $3400 \text{ \AA} < \lambda < 4100 \text{ \AA}$.

Supplementing these data are ACS frames covering the galaxies' rest-frame UV continuum. Specifically, we examined data taken through the F435W, F606W, F775W, F814W, and F850LP filters, which, for our oELGs and $z \sim 2.1$ LAEs, span the rest-frame wavelengths from $\sim 1300 \text{ \AA}$ to $\sim 3000 \text{ \AA}$, depending on the exact redshift. For the $z \sim 3.1$ LAEs, the F435W filter is excluded from our analysis, as it lies blueward of Ly α and may be affected by intervening hydrogen absorption (Madau 1995). The remaining filters extend from just redward of Ly α to about 2300 \AA . These ACS data reach depths comparable to that of the F160W data, but have a better drizzled image scale of $0''.03$ per pixel.

4. MEASURING SIZE AND CONCENTRATION

The structural properties of our $z \gtrsim 2$ galaxies were measured using a reduction pipeline very similar to that developed by Bond et al. (2009) for the analysis of rest-frame UV images. We began with the WFC3 F160W frames and extracted an $18'' \times 18''$ postage-stamp region around each galaxy. We then identified all possible sources within each galaxy cutout by using the SExtractor catalog builder (Bertin & Arnouts 1996) with extraction parameters DETECT_MINAREA = 30, DEBLEND_MINCONT = 0.06, and a uniform background. A second SExtractor pass, this time with DETECT_MINAREA = 5, was employed to compute the flux-weighted centroid of each object.

We note that in this particular analysis of $z \gtrsim 2$ galaxy morphology, the identification of F160W counterparts to our emission-line selected galaxies was not an issue. For the oELGs, which were originally selected using the G141 infrared grism on the WFC3, the identification of the F160W source was part of the discovery and spectral extraction process (Zeimann et al. 2014). For the LAEs, the formal $\sim 0''.25$ astrometric uncertainty of the MUSYC frames was confirmed by Bond et al. (2009) during their analysis of LAEs on *HST* rest-frame UV images. With this precision (~ 4 pixels on the archival F160W frames), there is little ambiguity as to the most likely counterpart. Finally, most of the galaxies studied in this program have data in at least six filters: F435W, F606W, F775W, F814W, F850LP, and F160W. This wide wavelength coverage, coupled with the requirement that the galaxy be well-detected ($S/N > 10$) on the F160W image, ensured that any source present in the discovery image was also detectable on multiple CANDELS frames.

Once the likely F160W counterparts were identified, we measured their sizes through a series of circular apertures centered on the galaxies' centroids in the F160W image. (Because of the relatively high signal-to-noise ratio of the detections, the choice of filter used for this centroiding has little effect on the analysis.) We then estimated each galaxy's Petrosian-like radius by calculating the radial distance at which the galaxy's local surface brightness, $I(r)$, falls to half the mean surface brightness contained within its aperture (Petrosian 1976). In other words,

$$\eta(r) = \frac{I(r)}{\langle I(< r) \rangle} = 0.5 \quad (1)$$

As this quantity is defined in terms of a surface brightness ratio, it is relatively insensitive to the depth of the image and thus a robust measure of size. Moreover, in almost all cases, the $\eta(r) = 0.5$ radius is very close to what would be derived for the galaxy's half-light radius, if the surface brightness profile were to be extrapolated to infinity (Bershady et al. 2000).

Along with size, we also computed each galaxy's compactness as viewed in the rest-frame optical. Following Kent (1985) we defined a system's concentration index using the ratio of radii enclosing 80% and 20% of the galaxy's light, i.e.,

$$C = 5 \log \left[\frac{r_{80\%}}{r_{20\%}} \right] \quad (2)$$

Through this definition, elliptical galaxies in the local universe would have values of $C \sim 5$, bulgeless spiral

galaxies would have $C \sim 3$, and a Gaussian profile would have $C = 2.1$ (Bershady et al. 2000).

Since cosmological surface-brightness dimming makes it difficult to measure the total luminosity of faint, distant galaxies, we again adapted a dimensionless ratio of surface brightnesses in our measurements of concentration. Conselice (2003) demonstrated that for intermediate redshift objects, the total magnitude of a galaxy is well approximated by the light contained within a radius that is 1.5 times that defined by $\eta = 0.2$, and it is this value we use to compute C .

Finally, we repeated the above analyses in the rest-frame ultraviolet, using the deep F435W, F606W, F775W, F814W and F850LP images of the fields. These data, which are drizzled to $0''.03$ per pixel, have roughly twice the resolution as the F160W frames, but reach a similar depth. These additional images allowed us to trace the behavior of concentration and size versus the wavelength of observation.

To estimate the uncertainties on our galaxy sizes, we used the results of Bond et al. (2012), who conducted a series of Monte Carlo simulations on the F814W images of the GOODS (Giavalisco et al. 2004), GEMS (Rix et al. 2004), and HUDF surveys. Their analysis showed that the fractional uncertainty in the measured half-light radius is related to the total flux, f , contained within an object by

$$\frac{\sigma_{r_e}}{r_e} = 0.54 \frac{\sigma_f}{f} \quad (3)$$

where σ_f is the pixel-to-pixel flux uncertainty derived from the weight map, i.e., $\sigma_f = \sqrt{1/W}$. We adopt this relation for measurements in all our filters.

5. RESULTS

Our size and concentration results for oELGs and LAEs in the F814W and F160W filters are presented in Tables 1 and 2. Figure 1 displays histograms of the half-light radii listed in these tables. Before interpreting these data, however, it is important to understand their limitations. The majority of the galaxies detected in our survey have small angular sizes and may be unresolved, even at *HST* resolution. To investigate this possibility, we determined the instrumental resolution of our images using Tiny Tim, the *HST*'s point-spread-function (PSF) modeling program (Krist et al. 2011). Using this software, we created a series of point source images through the ACS/F814W and WFC3/F160W filters and measured their half-light radii in exactly the same manner as for our galaxies. These simulations reveal that objects with r_e less than 2.8 pixels ($0''.083$) in the ACS's F814W filter and 2.4 pixels ($0''.14$) in WFC3's F160W filter have sizes consistent with that of the median value of our modeled point sources. Any galaxy with a value of r_e smaller than these limits should therefore be treated as unresolved. In Figure 1, the resolution limits are shown as a dotted line (for the F814W frames) and a dashed line (for the F160W data).

As is apparent from Figure 1, virtually all of the $z \sim 2$ star-forming galaxies present in our sample are (at least marginally) resolved at rest-frame ultraviolet wavelengths. However, when viewed at longer wavelengths with the $0''.06$ per pixel plate scale of the WFC3's infrared camera, more than half ($\sim 60\%$) of our targets

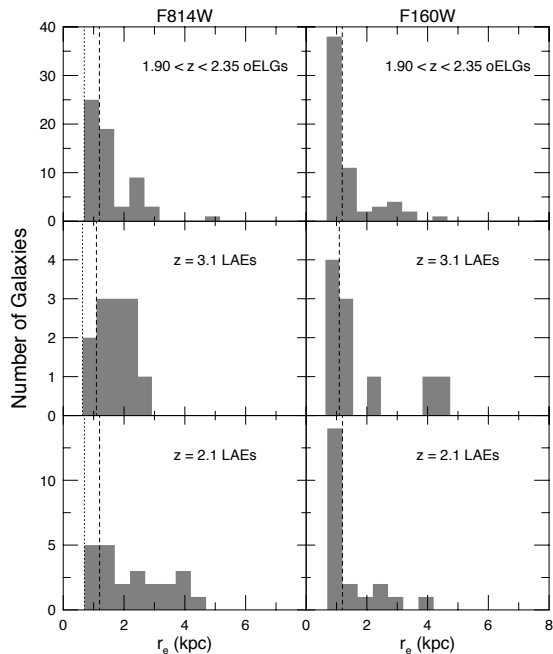


FIG. 1.— Distribution of half-light radii for oELGs and LAEs in the rest frame UV (F814W; left) and the rest frame optical (F160W; right). The dashed (F160W) and dotted (F814W) lines show the limits of our ability to resolve objects, given *HST*’s PSF and the finite pixel size of the instruments. The LAE size distributions are consistent with that found for the oELGs. Note that 62 out of the 96 galaxies are unresolved on the F160W frames; if the F160W sizes were the same as that seen through the F814W filter, only 34 of the galaxies would be unresolved.

have profiles consistent with that of a point source. For the LAEs, only 12 of the 35 ($\sim 34\%$) are resolved at WFC3 resolution, while for the oELGs the fraction is 21 out of 61 (again, $\sim 34\%$). Although this limitation prevents us from probing the full range of rest-frame optical morphologies exhibited by our $z \gtrsim 2$ emission-line sources, we can still use the data to draw conclusions about the epoch’s star-forming population.

The first conclusion arises from the similarity between the size distribution of LAEs and that found for galaxies identified via their rest-frame optical emission lines. A Kolmogorov-Smirnov (K-S) test can find no statistically significant difference in the distributions, either in the UV or in the optical. The same is true for the galaxies’ concentration index, which typically falls between 2 and 3: the distribution of C values for LAEs is statistically indistinguishable from that of oELGs. Although the number of Ly α emitters in our study is relatively small, the result does confirm the analysis of Hagen et al. (2016), who showed that galaxies selected on the basis of their Ly α emission have very similar properties to those of systems found via their rest-frame optical emission lines. Our concentration indices of LAEs in the rest-frame UV also match those of Gronwall et al. (2011), who measured the same quantity in $z \sim 3$ LAEs.

A second result comes from the wide-range of sizes exhibited by our emission-line selected galaxies. Although the bulk of the galaxy population is extremely compact, with half-light radii less than ~ 2 kpc, there is a tail to the distribution that extends to almost 6 kpc. Interestingly, this spread is not entirely driven by stellar mass. As Figure 2 illustrates, there is a correlation between

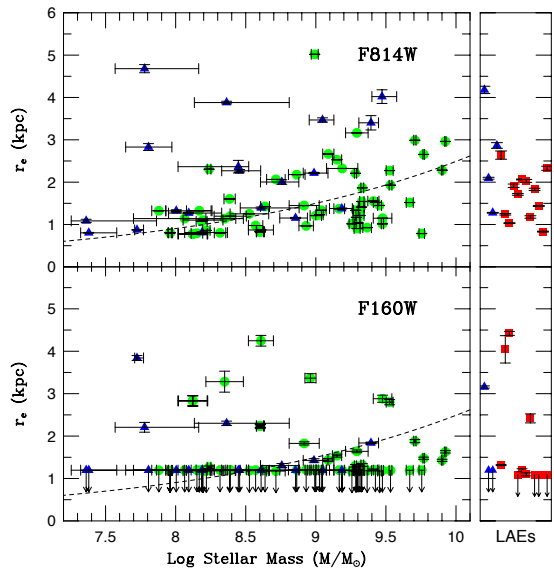


FIG. 2.— The stellar mass-half-light radius relationship for $2 \lesssim z \lesssim 3$ star-forming galaxies in the F160W and F814W filters. The oELGs are green circles, the $z \sim 2$ LAEs are blue triangles, and the $z \sim 3.1$ LAEs are shown as red squares. The stellar mass measurements come from Vargas et al. (2014) and Hagen et al. (2016); the dashed line shows the mean size-mass relation derived by van der Wel et al. (2014) for $z \sim 2.25$ star-forming galaxies. In the rest-frame UV, galaxy size does correlate with stellar mass, but with a large amount of scatter. While a size-mass relation may exist in the rest-frame optical, the poorer resolution of the IR data currently precludes its measurement. The panels on the right show LAEs without stellar mass measurements.

radius and stellar mass, but the scatter about the relation is substantial. At the high-mass end ($M \gtrsim 10^9 M_\odot$), our rest-frame UV results are consistent with the analysis of van der Wel et al. (2014), who have traced the $0 < z < 3$ evolution of the size-mass distribution using continuum-selected CANDELS galaxies with photometric results. Our results also agree with the measured the sizes and masses of $z = 2.53$ Ly α and H α selected galaxies with $M \gtrsim 10^8 M_\odot$ (Shimakawa et al. 2016). Unfortunately, while we would like to derive a similar relation for the galaxies in the rest-frame optical, the limited resolution of the *HST*’s WFC3 IR camera currently precludes this possibility.

The fact that many of our $z \gtrsim 2$ emission-line galaxies cannot be resolved in the F160W frames leads to the most important result of this study: most of the galaxies analyzed in this program have smaller half-light radii in the rest-frame optical than they do in the rest-frame ultraviolet. This result is displayed vividly in Figure 3, where we plotted the rest-frame UV half-light radius of each galaxy, as derived from their median size on the F435W, F606W, F775W, F814W, and F850LP frames, against their half-light radius in F160W. The offset in the sizes is obvious. The relation is not perfect, and some galaxies are larger in the rest-frame optical than they are in the UV. Nevertheless, the result is striking, and demonstrates that the star-forming regions detected by the rest-frame UV images of *HST* are not simply knots imbedded in larger, somewhat older systems.

The difference between the rest-frame optical and rest-frame UV sizes can be quantified using the Kaplan-Meier estimator for the empirical cumulative distribution function (Kaplan & Meier 1958). This estimator accounts

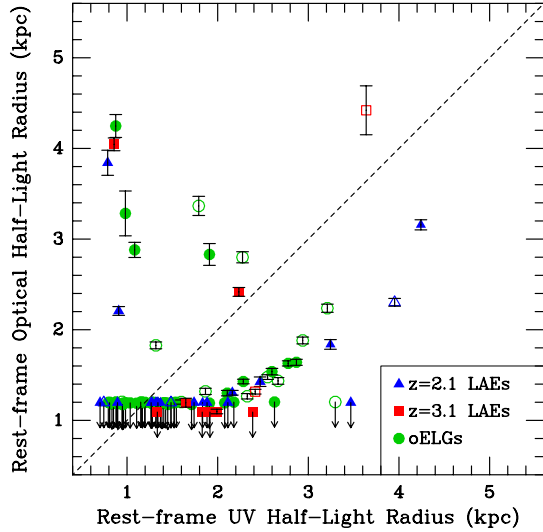


FIG. 3.— The half-light radii of our $z \gtrsim 2$ star-forming galaxies in rest-frame optical (WFC3/F160W) vs. similar measurements made in the rest-frame UV using ACS images in F435W, F606W, F775W, F814W, and F850LP. As in Figure 2, green circles represent the galaxies identified via their rest-frame optical emission lines, blue triangles show the $z \sim 2.1$ LAEs, and red squares denote the $z \sim 3.1$ LAEs. The open symbols denote objects with companions projected within $0''.6$. All unresolved galaxies in F160W are indicated as upper limits at the half-light radius of the instrument’s PSF. The vast majority of galaxies are smaller in the rest-frame optical than the rest-frame UV.

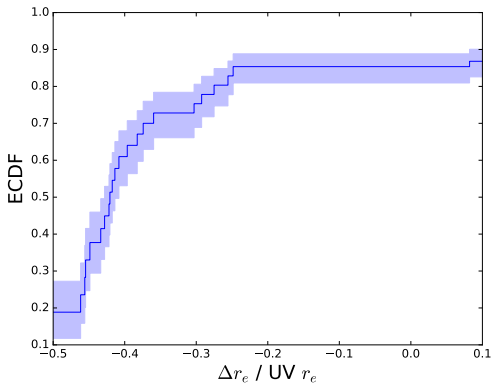


FIG. 4.— The Kaplan-Meier empirical cumulative distribution function (ECDF) for our combined sample of $z \gtrsim 2$ oELGs plotted against the fractional change in size of the galaxy between the rest-frame optical and rest-frame UV, i.e., $(r_e(\text{Opt}) - r_e(\text{UV})) / r_e(\text{UV})$. The shaded area denotes the 1σ confidence interval. The median fractional change between the rest-frame UV and optical is -0.40 , and $\sim 85\%$ of our galaxies are smaller at longer wavelengths.

for the existence of censored data (i.e., points with only upper limits), and calculates 1σ confidence intervals on the solution using a method developed by Greenwood (1926). (See Chapter 10 of Feigelson & Babu for more on information on the analysis of censored data.) The results of the Kaplan-Meier test are shown in Figure 4. From the figure, it is apparent that $\sim 85\%$ of our oELGs and LAEs are smaller in the rest-frame optical than they are in the UV, and that the median fractional change in r_e is 40%.

This wavelength shift in the appearance of our $z \gtrsim 2$ emission-line galaxies is also reflected in the systems’

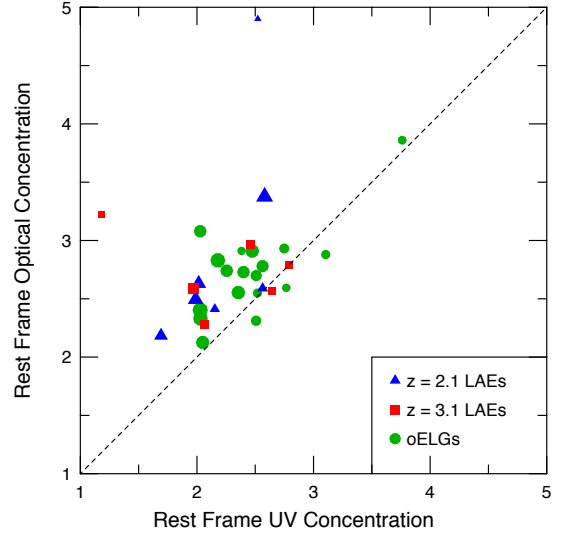


FIG. 5.— The Kent (1985) concentration index measured in the rest-frame ultraviolet compare to that derived from the rest-frame optical for $2 \lesssim z \lesssim 3$ star-forming galaxies. The plotting scheme is the same as Figures 2. The sizes of the points are proportional to how extended the galaxies appear on the sky. Only those galaxies that have been resolved on both the F160W and F814W frames have been included in the figure. All three samples of galaxies are more concentrated in the rest-frame optical than the rest-frame UV; this result is consistent with what is inferred from the galaxy’s half-light radii. The discrepancy in the sizes and concentrations suggests an inside-out scenario for galaxy formation.

mean concentration index. The majority of the galaxies in our dataset are unresolved on the F160W frames, and hence their concentrations are undefined. However, if we only consider those objects which are resolved, there is a systematic change in their structure with wavelength. Specifically, as Figure 5 illustrates, both the oELGs and LAEs appear more concentrated in the rest-frame optical than in the UV by a median value of $\Delta C = 0.21$. Moreover, this offset is not due to issues associated with small, semi-resolved objects, as the effect is larger in the more extended galaxies. Thus, the behavior we observe in the local universe, with galaxies appearing less concentrated in the ultraviolet, is mimicked at high- z .

Could those objects which appear larger in the rest-frame optical than in the UV be associated with mergers? To investigate this possibility, we used the CANDELS catalog to compute the surface density of objects present on the images, and then increased this number by $\sim 15\%$ to account of possible sources that are present in our SExtractor catalog but below the CANDELS limit. Based on this density, objects projected within $0''.6$ of any program galaxy have less than a 10% chance of being a chance superposition. Those objects with companions satisfying this criterion are shown in Figure 3 as open symbols. As one can see from the figure, close-by companions are principally associated with large systems: although $\sim 20\%$ of the $z \gtrsim 2$ star-forming galaxies studied in this program have neighbors superposed within $0''.6$, six out of our eight largest systems ($r_e(\text{UV}) \gtrsim 3$ kpc) belong to this subset. Less clear is the evidence for associating the $r_e(\text{Opt}) > r_e(\text{UV})$ galaxies with mergers: just 1/3 of those systems have nearby companions. Thus, it is possible that galaxy interactions may have an affect on the rest-frame optical sizes of star-forming galaxies, but the signal is weak at best.

5.1. Checking for Systematics

Figures 1, 3, and 4 all demonstrate that our $z \gtrsim 2$ star forming galaxies appear smaller at observer’s frame infrared wavelengths than in the observer’s frame optical. This behavior is opposite to the effect produced by diffraction, and the opposite of that expected from localized starbursts within the galaxies, where the UV may be emitted in just a few star forming regions. But it is still possible that the offset is due to an instrumental systematic or a product of our reduction procedures. To test for such effects, we undertook a series of experiments to explore the effects of image depths, binning, and wavelength on the results.

To test for a systematic error due to image depth, we added variable amounts of Gaussian noise to our images, and re-measured the half-light radii of the galaxies as a function of this noise. This analysis indicates that even when the signal-to-noise ratio is decreased by a factor of 30, there is no bias in our size measurements. (The precision of our estimated radii decreases, of course, as there is much greater scatter in the computed half-light radii. However, the values of r_e remain unbiased.) This result suggests that our conclusions are not being biased due to variations in the depths of the images.

The $0''.06$ per pixel image scale of the WFC3’s IR camera is twice as large as that for the ACS, which was used for all the other bandpasses in this study. To test whether this observational constraint has any affect on our results, we ran a 2×2 boxcar smoothing algorithm over our ACS F814W frames (to mimic the effect of the drizzled images’ correlated noise), binned the resultant image 2×2 , and remeasured the sizes of our galaxies. The result is that the half-light estimates on the more coarsely binned frames are $\sim 5\%$ larger than those on the original image. (This result is true even if we do not smooth prior to binning.) Thus, the effect of the larger pixel size is opposite that needed to explain the offset between observing windows.

Finally, we can examine the behavior of r_e with wavelength using solely the CCD data from the ACS. The ACS images range over 4000 \AA in the observed frame, and, for objects at $z \sim 2.1$, extend from the far UV ($\sim 1400 \text{ \AA}$) to the very near UV ($\sim 3000 \text{ \AA}$). This bandpass may be just large enough to check for a wavelength dependence on galaxy size that is independent of the WFC3 instrument.

Figure 6 illustrates the results of this experiment by plotting the Pearson correlation coefficient derived for a size versus wavelength regression against F814W half-light radius. For the oELGs and $z \sim 2.1$ LAEs, measurements through the ACS’s F435W, F606W, F775W, F814W, and F850LP filters all went into deriving the correlation coefficient, while for the $z \sim 3.1$ LAEs, the bluest filter was omitted from the analysis (due to it lying blue ward of Lyman- α). For the smallest objects, i.e., those with radii only slightly larger than the frame’s point spread function, there is little evidence for systematic behavior: if anything, the galaxies become larger with wavelength, as might be expected if the PSF were dominated by diffraction effects. However, for the larger galaxies, there is clear evidence for an inverse correlation between the wavelength of observation and size. Again, this result supports our conclusion that emission-

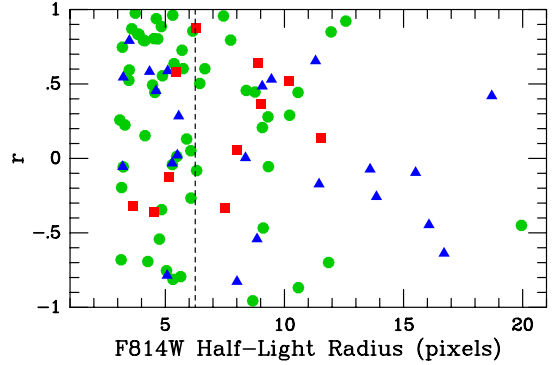


FIG. 6.— The y -axis displays the Pearson correlation coefficient, r , derived from a regression of half-light radii measured in five of the ACS’s filters (F435W, F606W, F775W, F814W, and F850LP). The x -axis shows the F814W half-light radius, plotted in pixels. The dotted line is drawn at 1.5 times the value of r_e one would derive for a point source. The plotting scheme is the same as Figure 2. (For $z = 3.1$ sample, the F435W measurement was removed from the analysis.) There is no strong evidence of any systematic behavior in the smallest objects, but in the larger systems, galaxy size is inversely correlated with the wavelength of observation.

line galaxies in the $2 \lesssim z \lesssim 3$ epoch are more extended in the rest-frame UV than they are in the optical.

6. DISCUSSION

There are three possible explanations for the shift in observed size for $2 \lesssim z \lesssim 3$ star-forming galaxies. Perhaps the simplest interpretation involves reddening due to dust. In the local universe, the measured effective radius of a galaxy decreases significantly with increasing wavelength (e.g., Kelvin et al. 2012; Vulcani et al. 2014; Lange et al. 2015). This is mostly due to internal extinction: as one moves inward in a galaxy, the surface density of dust increases, leading to an increase in obscuration, especially in the ultraviolet. The result is a shift in the balance of total flux towards larger radii, which artificially increases the half-light radius (e.g., Möllenhoff et al. 2006; Graham & Worley 2008; Popescu et al. 2011). The same effect may be in play at the redshifts of our galaxies.

To test for this possibility, we used the slope of the galaxies’ UV spectral energy distribution (β), which has been measured for all the oELGs in our sample (Hagen et al. 2016). In general, the stellar extinction in these galaxies is rather low: if we adopt $\beta_0 = -2.25$ as the expected UV slope from an unreddened starburst population (Calzetti 2001), then the median value of $\Delta\beta = 0.5$ translates into a stellar differential extinction of only $E(B - V) = 0.11$ (Calzetti et al. 2000). Moreover, there is no significant correlation between $\Delta\beta$ and Δr_e . This strongly suggests that reddening is not responsible for the smaller values of optical r_e .

Alternatively, one might argue that our measurements are affected by the presence of active galactic nuclei (AGN). This explanation is extremely unlikely. Gronwall et al. (2007) and Ciardullo et al. (2012) have tested for AGN activity in our samples of ECDF-S LAEs by excluding objects detected in X-rays and by performing a deep X-ray stacking analysis on the objects. Furthermore, Zeimann et al. (2014) reported that, while low-luminosity AGN could be present in some of our oELGs, their contribution to the rest-frame UV continuum and the rest-frame optical emission lines must be very small.

Finally, any AGN that would be bright and unobscured enough to affect the distribution of optical light would most likely be even brighter in the UV, thereby shortening the half-light radii. This effect would work against the trend we observe.

Finally, the shift of r_e with wavelength may arise from a gradient in the stellar population. Inside-out models of galaxy formation predict that older stars should condense towards the centers of galaxies, perhaps in a bulge or pseudo-bulge (van den Bosch 1998; Dekel et al. 2009; Agertz et al. 2011). Inside-out formation has previously been observed in massive galaxies of the $z \sim 2$ epoch (e.g., Patel et al. 2013; Lang et al. 2014), and for $M \gtrsim 10^9 M_\odot$ galaxies at $z \sim 1$ (Bond et al. 2014; van der Wel et al. 2014; Nelson et al. 2013, 2016). Here, we see that the process is also at work in $z \sim 2$ galaxies with much lower stellar masses, $7.5 \lesssim \log_{10} M_*/M_\odot \lesssim 10$. Our results suggest that even the low-mass galaxies of the epoch are beginning to form a bulge or pseudo-bulge, with older stars concentrated in the middle of the galaxy. This is unexpected, since van der Wel et al. (2014) found that the effective size as a function of wavelength was itself a strong function of mass, and the change was negligible for low-mass galaxies. However, the stellar mass limit of van der Wel et al. (2014) is $\sim 10^9$, and so their analysis does not probe much of the mass range analyzed here.

The next steps towards understanding the morphological properties of low-mass galaxies in the $z \gtrsim 2$ universe are to vary the sample selection and broaden the redshift range. A proper investigation of structure will then require the improved depth and spatial resolution of

the Near-Infrared Camera (NIRcam) on the James Webb Space Telescope (JWST; Gardner et al. 2006; Horner & Rieke 2004; Rieke 2011). The near-infrared PSF of NIRcam will cover $0''.05$, which corresponds to a $z \sim 2$ spatial scale of 0.5 kpc. We look forward with anticipation to JWST's launch and science operations.

Support for program #AR-13234 was provided by NASA through a grant from the Space Telescope Science Institute, which is operated by the Association of Universities for Research in Astronomy, Inc., under NASA contract NAS 5-26555. This work is based on observations made with the NASA/ESA Hubble Space Telescope which is operated by the Association of Universities for Research in Astronomy, Inc., under NASA contract NAS5-26555. The data were obtained from the Hubble Legacy Archive, which is a collaboration between the Space Telescope Science Institute (STScI/NASA), the Space Telescope European Coordinating Facility (ST-ECF/ESA) and the Canadian Astronomy Data Centre (CAD/CRC/CSA).

The Institute for Gravitation and the Cosmos is supported by the Eberly College of Science and the Office of the Senior Vice President for Research at the Pennsylvania State University. This research has made use of NASA's Astrophysics Data System and the python packages IPython, AstroPy, NumPy, SciPy, lifelines, pandas, matplotlib, and photutils. (Pérez & Granger 2007; Astropy Collaboration et al. 2013; van der Walt et al. 2011; Jones et al. 2016; Davidson-Pilon 2016; McKinney 2010; Hunter 2007; Bradley et al. 2016).

REFERENCES

- Acquaviva, V., Gawiser, E., & Guaita, L. 2011, *ApJ*, 737, 47
- Adelberger, K.L., Steidel, C.C., Pettini, M., et al. 2005, *ApJ*, 619, 697
- Agertz, O., Teyssier, R., & Moore, B. 2011, *MNRAS*, 410, 1391
- Astropy Collaboration, Robitaille, T.P., Tollerud, E.J., et al. 2013, *A&A*, 558, A33
- Beckwith, S.V.W., Stiavelli, M., Koekemoer, A.M., et al. 2006, *AJ*, 132, 1729
- Bennett, C.L., Larson, D., Weiland, J.L., et al. 2013, *ApJS*, 208, 20
- Bershady, M.A., Jangren, A., & Conselice, C.J. 2000, *AJ*, 119, 2645
- Bertin, E., & Arnouts, S. 1996, *A&AS*, 117, 393
- Bond, N.A., Gawiser, E., Gronwall, C., et al. 2009, *ApJ*, 705, 639
- Bond, N.A., Gawiser, E., & Koekemoer, A.M. 2011, *ApJ*, 729, 48
- Bond, N.A., Gawiser, E., Guaita, L., et al. 2012, *ApJ*, 753, 95
- Bond, N.A., Gardner, J.P., de Mello, D.F., et al. 2014, *ApJ*, 791, 18
- Bouwens, R.J., Illingworth, G.D., Oesch, P.A., et al. 2011, *ApJ*, 737, 90
- Bradley, L., Sipocz, B., Robitaille, T., Tollerud, E., Deil, C., et al. 2013, *astropy/photutils v0.2.2*. Zenodo. <http://doi.org/10.5281/zenodo.155353>
- Brammer, G.B., van Dokkum, P.G., Franx, M., et al. 2012, *ApJS*, 200, 13
- Brinchmann, J., Abraham, R., Schade, D., et al. 1998, *ApJ*, 499, 112
- Calzetti, D. 2001, *PASP*, 113, 1449
- Calzetti, D., Armus, L., Bohlin, R.C., et al. 2000, *ApJ*, 533, 682
- Ciardullo, R., Gronwall, C., Wolf, C., et al. 2012, *ApJ*, 744, 110
- Conselice, C.J. 2003, *ApJS*, 147, 1
- Conselice, C.J., Blackburne, J.A., & Papovich, C. 2005, *ApJ*, 620, 564
- Daddi, E., Cimatti, A., Renzini, A., et al. 2004, *ApJ*, 617, 746
- Davidson-Pilon, C. 2016, Github repository, <https://github.com/CamDavidsonPilon/lifelines>
- Dekel, A., Sari, R., & Ceverino, D. 2009, *ApJ*, 703, 785
- Dickinson, M. 2000, *Philosophical Transactions of the Royal Society of London, Series A*, 358, 2001
- Ellis, R.S., McLure, R.J., Dunlop, J.S., et al. 2013, *ApJ*, 763, L7
- Elmegreen, B.G., & Elmegreen, D.M. 2005, *ApJ*, 627, 632
- Feigelson, E. D., & Babu, G. J. 2012. *Modern Statistical Methods for Astronomy: With R Applications*, (Cambridge: Cambridge University Press)
- Ferguson, H.C., Dickinson, M., Giavalisco, M., et al. 2004, *ApJ*, 600, L107
- Gardner, J.P., Mather, J.C., Clampin, M., et al. 2006, *Space Sci. Rev.*, 123, 485
- Gawiser, E., van Dokkum, P.G., Herrera, D., et al. 2006, *ApJS*, 162, 1
- Gawiser, E., Francke, H., Lai, K., et al. 2007, *ApJ*, 671, 278
- Giacconi, R., Rosati, P., Tozzi, P., et al. 2001, *ApJ*, 551, 624
- Giavalisco, M., Steidel, C.C., & Macchetto, F.D. 1996, *ApJ*, 470, 189
- Giavalisco, M. 2002, *ARA&A*, 40, 579
- Giavalisco, M., Ferguson, H.C., Koekemoer, A.M., et al. 2004, *ApJ*, 600, L93
- Glazebrook, K., Ellis, R., Santiago, B., & Griffiths, R. 1995, *MNRAS*, 275, L19
- Graham, A.W., & Worley, C.C. 2008, *MNRAS*, 388, 1708
- Grasshorn Gebhardt, H.S., Zeimann, G.R., Ciardullo, R., et al. 2016, *ApJ*, 817, 10
- Greenwood, M. 1926, *Reports on Public Health and Medical Subjects*, 33, 1
- Griffiths, R.E., Ratnatunga, K.U., Casertano, S., et al. 1996, *I.A.U. Symp. 168: Examining the Big Bang and Diffuse Background Radiations*, ed. M. Kafatos & Y. Kondo (Dordrecht: Kluwer), 219

- Groggin, N.A., Kocevski, D.D., Faber, S.M., et al. 2011, *ApJS*, 197, 35
- Gronwall, C., Ciardullo, R., Hickey, T., et al. 2007, *ApJ*, 667, 79
- Gronwall, C., Bond, N.A., Ciardullo, R., et al. 2011, *ApJ*, 743, 9
- Guaia, L., Gawiser, E., Padilla, N., et al. 2010, *ApJ*, 714, 255
- Guaia, L., Acquaviva, V., Padilla, N., et al. 2011, *ApJ*, 733, 114
- Hagen, A., Ciardullo, R., Gronwall, C., et al. 2014, *ApJ*, 786, 59
- Hagen, A., Zeimann, G.R., Behrens, C., et al. 2016, *ApJ*, 817, 79
- Horne, S.D., & Rieke, M.J. 2004, *Proc. SPIE*, 5487, 628
- Hubble, E.P. 1936, *Realm of the Nebulae* (New Haven: Yale University Press)
- Hunter, J.D., 2007, *Computing in Science & Engineering*, 9, 90
- Jones, E., Oliphant, E., Peterson, P., et al. 2016, *SciPy: Open Source Scientific Tools for Python*, <http://www.scipy.org>
- Kaplan, E. L., & Meier, P. 1958, *J. Amer. Statist. Assn.* 53 (282), 457
- Kelvin, L.S., Driver, S.P., Robotham, A.S.G., et al. 2012, *MNRAS*, 421, 1007
- Kent, S.M. 1985, *ApJS*, 59, 115
- Koekemoer, A.M., Faber, S.M., Ferguson, H.C., et al. 2011, *ApJS*, 197, 36
- Krist, J.E., Hook, R.N., & Stoehr, F. 2011, *Proc. SPIE*, 8127, 81270J
- Lang, P., Wuyts, S., Somerville, R.S., et al. 2014, *ApJ*, 788, 11
- Lange, R., Driver, S.P., Robotham, A.S.G., et al. 2015, *MNRAS*, 447, 2603
- Lehmer, B.D., Brandt, W.N., Alexander, D.M., et al. 2005, *ApJS*, 161, 21
- Lilly, S., Schade, D., Ellis, R., et al. 1998, *ApJ*, 500, 75
- Lotz, J.M., Madau, P., Giavalisco, M., Primack, J., & Ferguson, H.C. 2006, *ApJ*, 636, 592
- Lowenthal, J.D., Koo, D.C., Guzmán, R., et al. 1997, *ApJ*, 481, 673
- Luo, B., Bauer, F.E., Brandt, W.N., et al. 2008, *ApJS*, 179, 19
- Madau, P. 1995, *ApJ*, 441, 18
- McKinney, W. 2010, *Proceedings of the 9th Python in Science Conference*, 51
- Möllenhoff, C., Popescu, C.C., & Tuffs, R.J. 2006, *A&A*, 456, 941
- Nelson, E.J., van Dokkum, P.G., Förster Schreiber, N.M., et al. 2016, *ApJ*, 828, 27
- Nelson, E.J., van Dokkum, P.G., Momcheva, I., et al. 2013, *ApJ*, 763, L16
- Papovich, C., Dickinson, M., Giavalisco, M., Conselice, C.J., & Ferguson, H.C. 2005, *ApJ*, 631, 101
- Pérez, F. & Granger, B. 2007, *Computing in Science & Engineering*, 9, 21
- Patel, S.G., van Dokkum, P.G., Franx, M., et al. 2013, *ApJ*, 766, 15
- Petrosian, V. 1976, *ApJ*, 209, L1
- Petty, S.M., de Mello, D.F., Gallagher, J.S., III, et al. 2009, *AJ*, 138, 362
- Pirzkal, N., Malhotra, S., Rhoads, J.E., & Xu, C. 2007, *ApJ*, 667, 49
- Popescu, C.C., Tuffs, R.J., Dopita, M.A., et al. 2011, *A&A*, 527, A109
- Quadri, R., van Dokkum, P., Gawiser, E., et al. 2007, *ApJ*, 654, 138
- Ravindranath, S., Ferguson, H.C., Conselice, C., et al. 2004, *ApJ*, 604, L9
- Ravindranath, S., Giavalisco, M., Ferguson, H.C., et al. 2006, *ApJ*, 652, 963
- Rieke, M. 2011, *Galaxy Evolution: Infrared to Millimeter Wavelength Perspective*, 446, 331
- Rix, H.-W., Barden, M., Beckwith, S.V.W., et al. 2004, *ApJS*, 152, 163
- Rodighiero, G., Daddi, E., Baronchelli, I., et al. 2011, *ApJ*, 739, L40
- Shimakawa, R., Kodama, T., Shibuya, T., et al. 2016, submitted to *MNRAS* (arXiv:1607.08005)
- Simard, L., Koo, D.C., Faber, S.M., et al. 1999, *ApJ*, 519, 563
- Stanford, S.A., Dickinson, M., Postman, M., et al. 2004, *AJ*, 127, 131
- Tacchella, S., Lang, P., Carollo, C.M., et al. 2015, *ApJ*, 802, 101
- Taylor-Mager, V.A., Conselice, C.J., Windhorst, R.A., & Jansen, R.A. 2007, *ApJ*, 659, 162
- Vargas, C.J., Bish, H., Acquaviva, V., et al. 2014, *ApJ*, 783, 26
- van den Bergh, S. 2001, *AJ*, 122, 621
- van den Bergh, S., Abraham, R.G., Ellis, R.S., et al. 1996, *AJ*, 112, 359
- van den Bosch, F.C. 1998, *ApJ*, 507, 601
- van der Walt, S., Colbert, S. and Varoquaux, G. 2011, *Computing in Science & Engineering*, 13, 22
- van der Wel, A., Franx, M., van Dokkum, P.G., et al. 2014, *ApJ*, 788, 28
- van Dokkum, P.G., Franx, M., Fabricant, D., Illingworth, G.D., & Kelson, D.D. 2000, *ApJ*, 541, 95
- Virani, S.N., Treister, E., Urry, C.M., & Gawiser, E. 2006, *AJ*, 131, 2373
- Vulcani, B., Bamford, S.P., Häußler, B., et al. 2014, *MNRAS*, 441, 1340
- Windhorst, R.A., Cohen, S.H., Hathi, N.P., et al. 2011, *ApJS*, 193, 27
- Zeimann, G.R., Ciardullo, R., Gebhardt, H., et al. 2014, *ApJ*, 790, 113

TABLE 1
oELG MORPHOLOGY RESULTS

Field	ID	$\alpha(2000)$	$\delta(2000)$	z	Concentration		Half Light Radii (arcsec)	
					F160W	F814W	F160W	F814W
30	272	53.07186	-27.82070	1.965	2.73	2.40	0.170 ± 0.003	0.272 ± 0.001
32	6417	53.14214	-27.83269	2.153	2.66	1.67	< 0.143	0.193 ± 0.001
34	2329	53.22949	-27.86480	2.171	2.88	3.10	0.348 ± 0.010	0.139 ± 0.001
35	3033	53.13376	-27.80791	1.964	3.61	3.35	< 0.143	0.598 ± 0.004
35	3485	53.14352	-27.79522	2.035	3.86	3.76	0.268 ± 0.005	0.099 ± 0.001
36	140	53.17578	-27.81656	2.079	2.87	2.59	< 0.143	0.137 ± 0.002
38	5800	53.13813	-27.86549	1.947	3.60	2.73	< 0.143	0.108 ± 0.001
38	8270	53.13007	-27.84289	1.940	3.02	2.98	< 0.143	0.115 ± 0.001
42	7854	53.18730	-27.89793	1.990	2.82	2.45	< 0.143	0.260 ± 0.003
42	8611	53.18976	-27.89537	2.059	2.65	2.48	< 0.143	0.164 ± 0.001
43	7274	53.09959	-27.93800	2.103	2.49	2.26	< 0.143	0.279 ± 0.002
44	7544	53.16297	-27.91688	2.136	2.94	2.31	< 0.143	0.232 ± 0.001
45	807	53.10760	-27.76926	2.076	2.69	2.79	< 0.143	0.171 ± 0.002
45	950	53.11179	-27.76718	2.079	2.75	2.89	< 0.143	0.169 ± 0.001
47	1069	53.05181	-27.84883	1.945	2.55	2.36	0.171 ± 0.004	0.318 ± 0.002
47	3211	53.07551	-27.82831	2.034	2.59	2.73	< 0.143	0.182 ± 0.001
48	366	53.10337	-27.84163	2.026	3.24	2.68	< 0.143	0.095 ± 0.001
49	3237	53.16832	-27.87671	2.098	3.08	2.03	0.336 ± 0.007	0.273 ± 0.001
49	3613	53.16614	-27.87466	2.131	2.60	2.55	< 0.143	0.122 ± 0.001
49	7054	53.18917	-27.86309	1.970	2.44	2.25	< 0.143	0.159 ± 0.001
50	6492	53.23087	-27.89474	1.939	2.55	2.52	0.391 ± 0.029	0.136 ± 0.003
50	6991	53.24629	-27.88908	2.031	2.70	2.51	0.158 ± 0.004	0.223 ± 0.001
50	7651	53.24427	-27.88427	2.318	3.28	2.07	< 0.143	0.252 ± 0.005
51	2927	53.03610	-27.71394	2.075	2.83	2.18	0.226 ± 0.004	0.359 ± 0.008
51	4972	53.01040	-27.71408	2.087	2.33	2.03	0.196 ± 0.003	0.356 ± 0.004
52	3988	53.04419	-27.76833	2.198	5.16	2.62	< 0.143	0.151 ± 0.003
53	3713	53.03542	-27.80838	2.012	2.71	2.92	< 0.143	0.096 ± 0.001
53	7617	53.04000	-27.79442	2.040	2.75	2.98	< 0.143	0.145 ± 0.001
53	10334	53.02820	-27.77938	1.958	3.96	3.41	< 0.143	0.143 ± 0.003
54	8192	53.08472	-27.86133	1.923	2.78	2.56	0.155 ± 0.004	0.263 ± 0.001
55	3245	53.19357	-27.84351	2.009	2.51	2.30	< 0.143	0.185 ± 0.001
55	6276	53.21752	-27.82591	2.211	2.74	3.11	< 0.143	0.112 ± 0.001
55	6384	53.19595	-27.82481	2.090	2.65	2.67	< 0.143	0.140 ± 0.001
55	6583	53.19229	-27.82294	2.032	2.47	2.45	< 0.143	0.145 ± 0.001
55	7946	53.20340	-27.81601	1.999	2.91	2.47	0.177 ± 0.003	0.317 ± 0.001
57	1058	53.18804	-27.74458	2.134	2.80	3.41	< 0.143	0.160 ± 0.004
57	2412	53.19244	-27.73599	1.969	2.40	2.03	0.196 ± 0.004	0.377 ± 0.003
57	2674	53.18128	-27.73417	1.946	2.45	2.35	< 0.143	0.146 ± 0.001
57	3737	53.19071	-27.72948	2.250	3.07	4.68	< 0.143	0.134 ± 0.003
57	4713	53.18109	-27.72681	2.078	2.60	2.58	< 0.143	0.182 ± 0.002
57	4879	53.17942	-27.72628	2.221	2.13	2.05	0.186 ± 0.004	0.306 ± 0.003
57	8227	53.18195	-27.71891	2.105	2.90	2.62	< 0.143	0.124 ± 0.001
59	217	53.09352	-27.80971	2.324	2.67	2.57	< 0.143	0.124 ± 0.001
59	951	53.09040	-27.80183	2.014	2.91	2.38	0.508 ± 0.015	0.104 ± 0.001
59	1736	53.08912	-27.79275	2.255	2.63	2.69	< 0.143	0.105 ± 0.001
59	2130	53.08884	-27.78168	1.947	2.93	2.75	0.218 ± 0.004	0.172 ± 0.001
59	3424	53.11297	-27.77869	2.239	2.74	2.26	0.154 ± 0.004	0.280 ± 0.008
60	247	53.14352	-27.79522	2.029	3.86	3.76	0.268 ± 0.005	0.099 ± 0.001
60	1017	53.13915	-27.78615	1.987	2.59	2.77	0.338 ± 0.014	0.093 ± 0.001
60	1362	53.12986	-27.78225	2.137	2.50	2.58	< 0.143	0.161 ± 0.001
60	2437	53.14781	-27.77136	2.175	2.92	2.97	< 0.143	0.097 ± 0.001
60	3248	53.14777	-27.76562	2.316	2.31	2.51	0.147 ± 0.003	0.189 ± 0.001
63	1506	53.16881	-27.79694	1.992	2.80	3.59	< 0.143	0.128 ± 0.001
63	1687	53.14832	-27.79594	2.030	2.87	2.70	< 0.143	0.117 ± 0.002
63	1756	53.14352	-27.79522	2.031	3.86	3.76	0.268 ± 0.005	0.099 ± 0.001
63	2814	53.13915	-27.78615	1.995	2.59	2.77	0.338 ± 0.014	0.093 ± 0.001
63	3188	53.18222	-27.78331	2.081	3.21	...	0.404 ± 0.013	...
63	3384	53.16746	-27.78183	2.069	3.26	2.75	< 0.143	0.159 ± 0.003
63	3907	53.14889	-27.77750	2.073	3.07	2.58	< 0.143	0.094 ± 0.001
63	5097	53.15381	-27.76730	2.317	2.71	2.84	< 0.143	0.177 ± 0.001
63	5562	53.14781	-27.77136	2.177	2.92	2.97	< 0.143	0.097 ± 0.001

TABLE 2
LAE MORPHOLOGY RESULTS

ID	$\alpha(2000)$	$\delta(2000)$	z	Concentration		Half Light Radii (arcsec)	
				F160W	F814W	F160W	F814W
35	53.09592	-27.95504	2.06	2.49	1.99	0.379 ± 0.003	0.501 ± 0.010
38	53.09076	-27.94879	2.06	3.27	2.49	< 0.143	0.251 ± 0.003
40	53.12550	-27.94153	2.06	2.18	1.69	0.220 ± 0.002	0.408 ± 0.020
50	53.12928	-27.91751	2.06	3.71	2.47	< 0.143	0.167 ± 0.003
55	53.18977	-27.89537	2.06	2.65	2.49	< 0.143	0.165 ± 0.001
60	53.06520	-27.87591	2.06	2.64	2.54	< 0.143	0.096 ± 0.001
66	53.08463	-27.85105	2.06	3.82	2.59	< 0.143	0.153 ± 0.001
68	53.04731	-27.84727	2.06	2.63	2.02	0.276 ± 0.006	0.465 ± 0.004
69	53.12413	-27.84367	2.06	2.59	2.56	0.171 ± 0.005	0.265 ± 0.002
70	53.04772	-27.84075	2.06	4.90	2.52	0.461 ± 0.007	0.105 ± 0.001
75	53.16885	-27.82570	2.06	2.87	1.79	< 0.143	0.284 ± 0.018
78	53.17580	-27.81655	2.06	2.85	2.61	< 0.143	0.138 ± 0.002
83	53.17307	-27.80679	2.06	3.88	2.74	< 0.143	0.097 ± 0.002
86	53.21541	-27.80223	2.06	2.33	4.04	< 0.143	0.130 ± 0.005
90	53.13286	-27.79795	2.06	5.21	1.81	< 0.143	0.339 ± 0.010
98	53.16750	-27.78188	2.06	2.64	2.58	< 0.143	0.159 ± 0.003
115	53.01718	-27.75078	2.06	3.17	3.09	< 0.143	0.152 ± 0.002
126	53.01668	-27.73100	2.06	3.38	2.58	0.265 ± 0.014	0.561 ± 0.011
130	53.18053	-27.72655	2.06	2.41	2.15	0.156 ± 0.006	0.240 ± 0.006
141	53.05732	-27.71680	2.06	6.24	1.93	< 0.143	0.272 ± 0.004
144	53.03030	-27.69660	2.06	...	1.78	...	0.482 ± 0.019
156	53.14160	-27.67207	2.06	2.82	1.93	< 0.143	0.416 ± 0.006
158	53.13110	-27.66999	2.06	...	2.79	...	0.344 ± 0.008
4	53.07833	-27.71338	3.12	2.59	1.97	0.173 ± 0.002	0.347 ± 0.013
6	53.21955	-27.80259	3.12	2.79	2.79	0.531 ± 0.042	0.163 ± 0.002
11	53.11215	-27.69116	3.12	3.22	1.18	0.581 ± 0.006	0.136 ± 0.001
16	53.05533	-27.72499	3.12	...	3.54	...	0.252 ± 0.005
22	53.16187	-27.69557	3.12	2.55	2.39	< 0.143	0.225 ± 0.003
25	53.16994	-27.76833	3.12	2.96	2.46	0.157 ± 0.005	0.271 ± 0.001
44	53.06578	-27.73618	3.12	2.28	2.07	0.144 ± 0.005	0.267 ± 0.005
56	53.14304	-27.79988	3.12	2.57	2.64	0.318 ± 0.014	0.155 ± 0.004
59	53.13857	-27.85766	3.12	2.80	2.50	< 0.143	0.240 ± 0.004
93	53.16438	-27.74711	3.12	2.69	2.84	< 0.143	0.189 ± 0.001
94	53.03884	-27.73179	3.12	...	2.35	...	0.109 ± 0.001
125	53.16256	-27.77286	3.12	2.01	2.18	< 0.143	0.306 ± 0.006